

# Studying the Effects of the August 2017 Solar Eclipse using LF/MF Signals of Opportunity

Marc A. Higginson-Rollins<sup>1</sup>, Morris B. Cohen<sup>1</sup>

<sup>1</sup>School of Electrical and Computer Engineering, Georgia Institute of Technology, 777 Atlantic Drive NW,  
Atlanta, GA 30332

## Key Points:

- Back scatter from the August 2017 solar eclipse is observed at around 300 kHz and used to estimate the  $h'$  and  $\beta$  of the totality spot.
- The width of the transition region between the totality spot and daytime ionosphere is estimated.
- The minimum required turn on time, or settling time, of totality spot boundary is estimated.

---

Corresponding author: Morris Cohen, [mcohen@gatech.edu](mailto:mcohen@gatech.edu)

## Abstract

We present observations and modeling of Low Frequency (LF; 30–300 kHz) and Medium Frequency (MF; 300–3000 kHz) signals during 21-August-2017 "Great American Solar Eclipse" using Nationwide Differential GPS (NDGPS) transmitters as a signal of opportunity. Apparent forward and back scattering from the eclipse totality spot is presented for the first time. The effect of the solar eclipse on the D-region electron density is investigated using FDTD modeling. The waveguide parameters of the totality spot are estimated to be  $h' = 80 \pm 3$  km and  $\beta = 0.9 \pm 0.1$  km<sup>-1</sup>. The transition from an obscured ionosphere to a fully eclipsed ionosphere may be slow, 10s of seconds, but the transition from a fully eclipsed ionosphere to obscured likely occurred quite fast, less than a second, when the Sun's influence reappeared.

## 1 Introduction

The D-region of the ionosphere, which ranges from about 60-100 km, is too high for continuous in-situ measurements, such as with high-altitude balloons, and too low for satellite-based measurements. Molecular oxygen and nitrogen, nitric oxide, and other atoms, such as sodium and calcium, constitute this layer of ionization (Nicolet & Aikin, 1960). The ionization in the D-region of the ionosphere is primarily due to Lyman- $\alpha$  radiation during the day and cosmic rays and Lyman- $\beta$  backscatter from the Earth's hydrogen exosphere at night (Kotovskiy & Moore, 2016). This ionization acts as a dispersive, anisotropic media that reflects lower frequency waves and attenuates higher frequencies.

Since the D-region (and the ground) reflects lower frequency waves efficiently, the region between the Earth and the D-region is often referred to as the "Earth-Ionosphere Waveguide". An effective and widespread method to study the D-region is through the use of Very Low Frequency (VLF, 3–30 kHz) and Low Frequency (LF, 30–300 kHz) radio waves from man-made transmitters, (e.g. (Füllekrug, Koh, Liu, & Mezentssev, 2019)), or natural sources (e.g. (McCormick, Cohen, Gross, & Said, 2018)), due to the efficient reflection of waves that allow propagation to global distances. As the frequency of the wave increase, the attenuation of the reflected signal increases as well, (Bickel, 1957), as does the reflection height. Waves between LF and Medium Frequencies (MF, 300–3000 kHz) reflect higher, with higher attenuation, but still reflect within the D-region and can

serve to complement VLF observations. Waves around 200–400 kHz have previously been used to monitor and study the D-region, (Belrose, Hatton, McKerrow, & Thain, 1959; Belrose & Thomas, 1968; Bickel, 1957; Clarke, 1962; C. McKerrow, 1957; C. A. McKerrow, 1960). Higginson-Rollins and Cohen (2017) found that the United States Coast Guard’s (USCG) Nationwide Differential Global Position System (NDGPS) can be used as a signal of opportunity for studying the D-region and captures perturbations typically associated with the D-region.

Previous research examining the effect of a total solar eclipse on the D-region has primarily been done using VLF techniques, (e.g. Kaufmann & Schaal, 1968; Schaal, Mendes, Ananthakrishnan, & Kaufmann, 1970). Work done by Sprenger, Lauter, and Schmelovsky (1962) examined the effect of two solar eclipses (30 June 1954 and 15 February 1961) on the D-region using frequencies between 191–1178 kHz. This work examined reflection heights and signal absorption for multiple transmitter-receiver paths during both events and found approximate values for the attachment and detachment processes during the event. On August 21, 2017, the "Great American Solar Eclipse" traversed the continental United States (CONUS). Using an array of radio receivers and VLF/LF transmitters, Cohen, Gross, et al. (2018) analyzed the signal change for a multitude of transmitter-receiver paths and detected a signature of direct scattering from the totality spot. This paper will complement previous research by: 1) presenting evidence of back scatter from the August 21, 2017, solar eclipse totality spot using NDGPS transmitters, 2) model the back scatter and use it to determine the "sharpness" of the totality spot, and 3) provide an estimate for the settling time of the D-region.

## 2 Data Collection and Interpretation

### 2.1 LF AWESOME Receivers

The data in this paper was collected using the LF AWESOME Receiver (Cohen, Said, et al., 2018). This instrument consists of two orthogonal air-core loop antennas and has a sampling rate of 1 MHz, giving a band-pass of approximately 0.5–470 kHz, sensitivity up to  $0.03 \text{ fT}/\sqrt{\text{Hz}}$  at 30 kHz and  $0.1 \text{ fT}/\sqrt{\text{Hz}}$  at 300 kHz, and RMS timing accuracy of 15–20 ns for the RMS accuracy of all the timing pulses that make up the 1 MHz clock (implying precise phase estimation of  $<1.5$  degrees at 300 kHz), there is no frequency drift/offset in the clock detectable with 0.5 part-per-billion resolution. The

Georgia Tech Low Frequency Lab currently operates a network of 11 receivers throughout the United States and Japan. The two receivers used for this paper are located at: 1) Baxley, Georgia, [31.8767° N, 82.3621° W], 2) Pisgah Astronomical Research Institute (PARI), North Carolina, [35.1996° N, 82.8719° W].

## 2.2 NDGPS Transmitters

The NDGPS network consists of 33 sites which broadcast, between 285–325 kHz, the difference between a known, fixed location and the received GPS coordinates to improve the accuracy of commercial GPS to centimeter accuracy (D. Last & Poppe, 1996; J. Last & Poppe, 1997; Wolfe, Judy, Haukkala, & Godfrey, 2000). From extensive measurements using multiple transmitters and receivers, it has been found that the transmitter clocks drift, which causes phase instability, limiting the usefulness of the phase data. Thus, in this paper, only amplitude metrics are considered. Three transmitters will be used for this paper: 1) New Bern, North Carolina, [35.1750° N, 77.0485° W], 2) Tampa, Florida, [27.8502° N, 82.5324° W], and 3) Bobo, Mississippi, [34.1152° N, 90.6912° W]. Respectively, the transmitters have a baud rate of 100 bits-per-second (BPS), 200 BPS, and 200 BPS, and a center frequency of 294 kHz, 312 kHz, and 297 kHz.

## 2.3 Data Interpretation

The receiver collects broadband data for both the North/South (N/S) and the East/West (E/W) channel. A synchronized minimum-shift keyed (MSK) demodulation is then applied to the broadband data, which converts the MSK modulated transmitter signal into a quasi-CW (continuous wave) signal. The result is that the horizontal magnetic flux density of a narrowband transmitter can be represented by the amplitude and (carrier) phase of the N/S and E/W channel. These four values can be written as two separate complex phasors that defines an ellipse centered at the origin. Measures can be derived from the resulting ellipse and include major axis length, minor axis length, right-hand circular polarization (RHCP), left-hand circular polarization (LHCP), ellipticity, tilt angle, and start phase. Synchronized MSK demodulation and the polarization ellipse method are both covered in great detail by Gross, Cohen, Said, and Gólkowski (2018). The work in this paper will primarily focus on the major axis length and the minor axis length. These parameters correspond to the transverse magnetic (TM) and transverse electric (TE) modes of the magnetic field respectively.

### 3 Observations

#### 3.1 Forward Scattering

In the context of D-region remote sensing using VLF, LF, or MF transmitters, forward scattering refers to scattering from a perturbation located between the transmitter and receiver. Thus, the scattered signal propagates “forward” and is detected by the receiver, e.g. Johnson, Inan, Lev-Tov, and Bell (1999). Figure 1 shows two examples of forward scattering from NDGPS transmitters during the 21-August-2017 solar eclipse. The leftmost panel shows a map of the two propagation paths being observed: 1) New Bern, NC, [35.175° N, 77.049° W] to Baxley, GA, at 294 kHz, and 2) Bobo, MS, [34.115° N, 90.691° W] to PARI, NC, at 297 kHz. The respective path lengths are 627.1 km and 726.6 km. The two center panels show the amplitude data for the transmitter in New Bern, NC, to Baxley, GA. The top panel shows the data for the major axis length and the bottom panel shows the data for the minor axis length, both are in units of decibel picoTesla, dB-pT. The right panels show the same data for the Bobo, MS, to PARI, NC, transmitter-receive path. The four vertical lines in each data panel, labeled T1–T4, correspond to the position of the totality spot in the map.

As the eclipse totality spot moves from northwest to southeast across both transmitter-receive paths there is a clear modification to the data plots in all four panels. Due to the higher frequency of the NDGPS transmitters, specifically 294 kHz or 297 kHz for the data presented, the phase interference observed in the major/minor axis length varies rapidly, as seen in both cases. This is primarily due to: 1) the shorter wavelength of 1 km and 2) the fewer propagating modes, (Higginson-Rollins & Cohen, 2017). This is most apparent in the path from Bobo to PARI when compared to the observations made in Cohen, Gross, et al. (2018). The major axis trend is different between the two plots, the NDGPS transmitter major axis length increases and then decreases as the eclipse totality spot moves across the propagation path with a fading pattern, peaks and nulls from phase interference, superimposed on top of it. The middle column showing propagation from New Bern, NC, to Baxley, GA, shows a more pronounced case of phase interference. As the eclipse spot moves across the path, both the major axis and minor axis have two peaks and a null from the phase interference, though the minor axis has a much broader peak than the major axis.

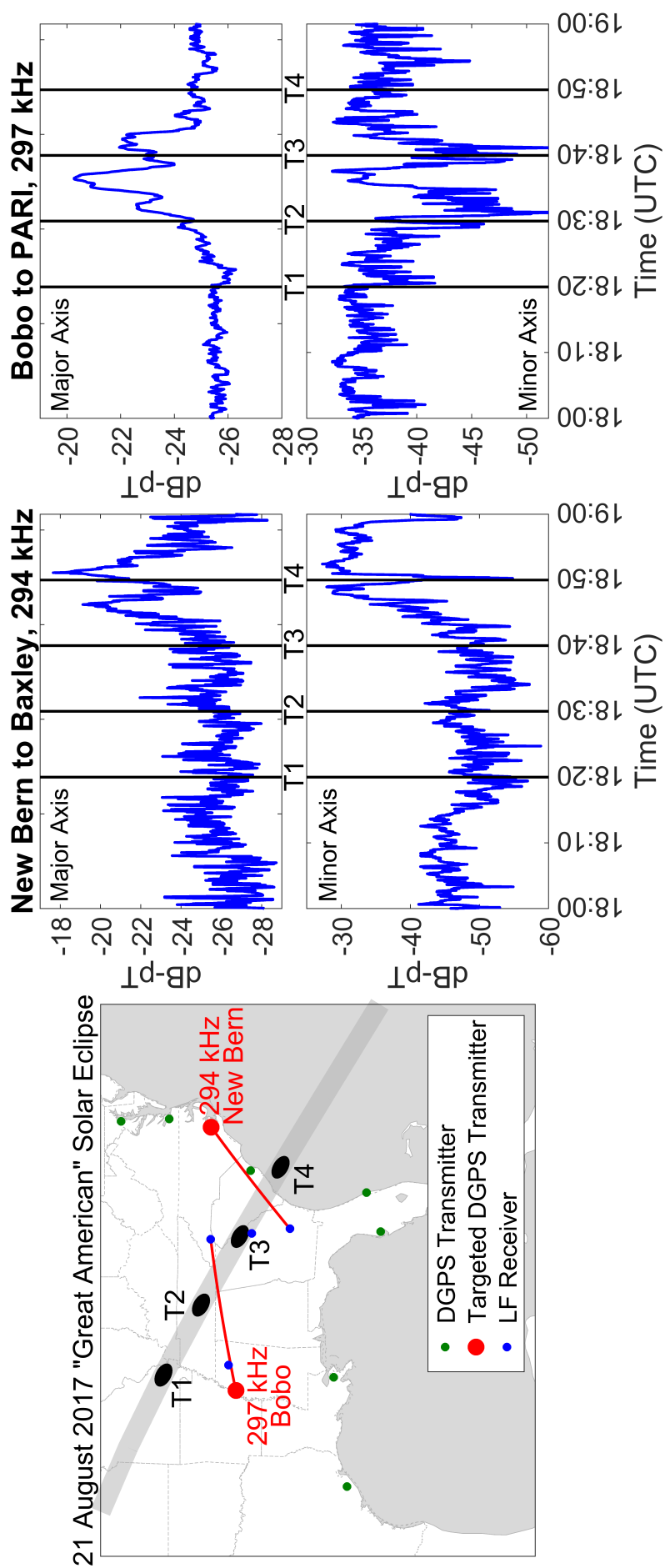


**Figure 1.** Map depicting the totality path of the eclipse (gray swath), the NDGPS transmitters (red and green), and the LF radio receivers (blue). The two red lines in the map are highlighted propagation paths shown in the center and right columns. The four black ellipses labeled T1-T4 are four highlighted positions of the eclipse totality spot. The times of these positions are shown in the two right columns and labeled accordingly.

### 3.2 Back Scattering

As opposed to forward scattering, back scattering occurs when the perturbation is “behind” the receiver. Thus, waves scattering off the perturbation propagate “backwards” and are detected by the receiver. Figure 2 shows an example of back scattering from NDGPS transmitters during the 21-August-2017 solar eclipse. The leftmost panel shows a map of the propagation path being observed: Tampa, FL, [27.8502° N, 82.5325° W] to Baxley, GA, at 312 kHz. The path length is 446.64 km. The two panels in the right column show the major and minor axis lengths in units of decibels of picoTesla, dB-pT, for this propagation path. The four vertical lines in both data panels, labeled T1–T4, correspond to the position of the totality spot in the map on the left. As the eclipse spot moves from northwest to southeast, the top right panel showing the major axis length appears to trend downward until it reaches T3, when a fading pattern appears. At T3 there is an enhancement in the major axis, i.e. a peak, followed by a null just before T4, at around 18:47 UTC. It’s important to note that the eclipse totality patch does not cross the propagation path, as seen in the map on the left. Thus, it appears that this modification is caused by back scattering from the eclipse spot.

An important consideration for any observations during the 21-August-2017 solar eclipse is that a solar flare occurred at approximately the same time, (Cohen, Gross, et al., 2018). Thus, care must be taken to ensure that the effect of the solar flare on the solar eclipse is accounted for. The bottom panel of Figure 2 shows the major axis length normalized to account for the solar flare. By comparing the eclipse day to a quiet day, it was ascertained that a slow linear decrease in the major axis was the effect that needs to be corrected. This is done by applying a linear fit to the downward trend that appears before the fading pattern, which is extrapolated to continue through the peak of the modification from the solar eclipse. The linear fit is then subtracted from the major axis length. The two dashed horizontal black lines show approximate values for the major axis length from the “quiet” D-region, bottom line, and from the perturbed D-region, top line. The difference between these two lines, labeled on the panel, is about 0.5 dB-pT, which is the enhancement to the major axis length resulting from the back scatter, with the effect of the solar flare removed. The 0.5 dB-pT enhancement near “T3” is assumed to be the back scattering from the solar eclipse totality spot because it is the approximate time when the totality spot is located directly behind the receiver, which is a required for modeling using a two-dimensional grid.

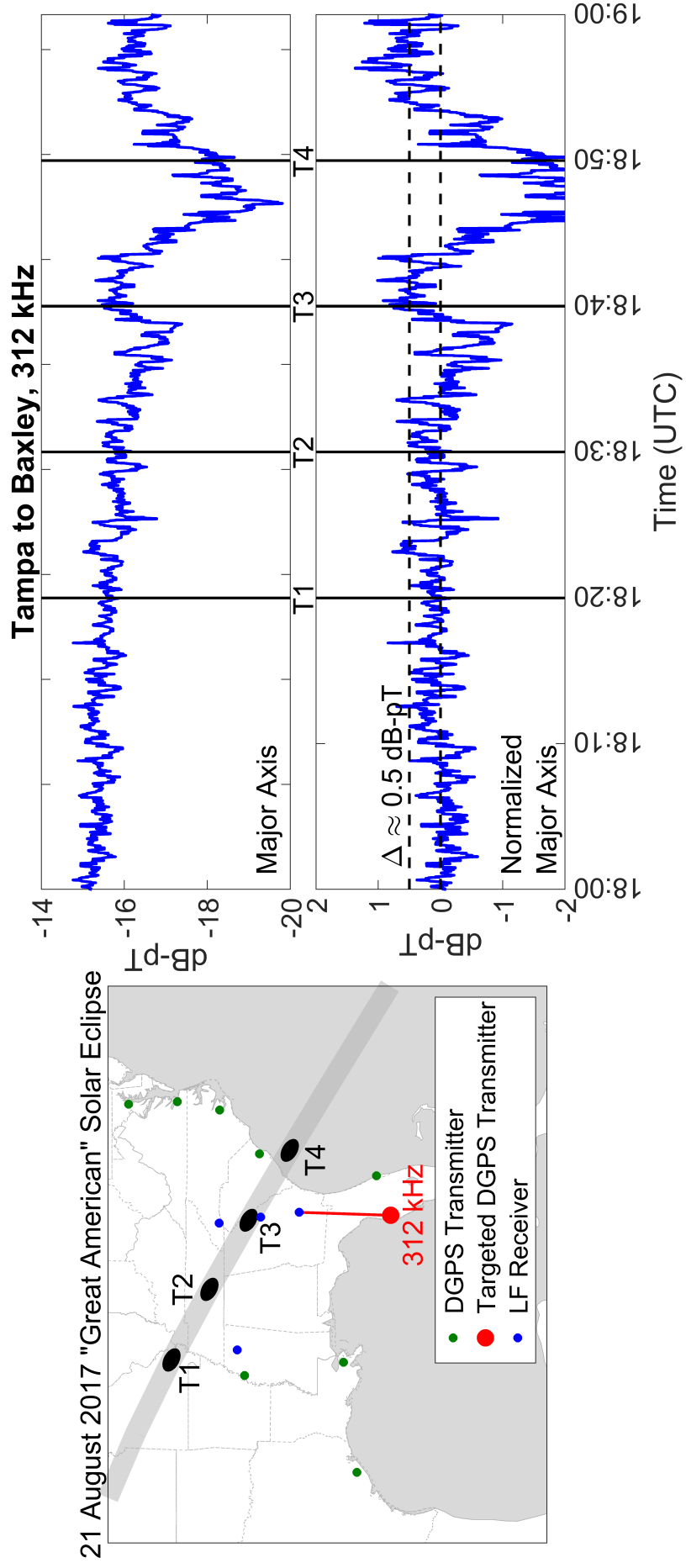


**Figure 2.** Map depicting the totality path of the eclipse (gray swath), the NDGPS transmitters (red and green), and the LF radio receivers (blue). The red line in the map is the highlighted propagation paths shown in the right columns. The four black ellipses labeled T1-T4 are four highlighted positions of the eclipse totality spot. The times of these positions are shown in the right column and labeled accordingly.



## 4 Back Scatter Modeling

The FDTD code used for this research has been adapted from the code provided by Dr. Robert Marshall at the University of Colorado at Boulder (e.g. Marshall, 2012; Marshall & Close, 2015). The "sharpness" of the totality spot of the eclipse can roughly be thought of as a function of two things: 1) the difference in electron density ( $N_e$  between the average daytime D-region and the center of the totality spot, and 2) the gradient of the difference in electron density. For the purpose of this work, the electron-neutral collision frequency profile was assumed to be constant.

A parameterization of the D-region electron density can be used to further simplify the number of input parameters. The parameterization from (Wait & Spies, 1964) will be used for this paper, see Equation 1. This function uses two parameters (or "waveguide parameters"),  $h'$  km and  $\beta$  km<sup>-1</sup>, to approximate the electron density of the D-region. An increase in  $h'$  may be thought of as the "y-intercept" of the D-region electron density moving (although not physically moving) in altitude, which is often associated with a reduction in ionization. The  $\beta$  variable can be thought of as the "slope" of the electron density in a logarithmic scale. An increase in  $\beta$  implies that the gradient of the electron density profile has increased. Typical waveguide parameters for the daytime D-region are a  $h' = 71$  km and  $\beta = 0.43$  km<sup>-1</sup>, Clilverd et al. (2001), which will be the values for the ionosphere outside the solar eclipse totality spot used in this work.

$$N_e(h) = 1.43 \cdot 10^{13} e^{-0.15h} e^{\beta(h-h')} \text{ m}^{-3} \quad (1)$$

The gradient of the difference in the electron density is varied by applying a smoothing window to the waveguide parameters. A window of 1 is equivalent to no smoothing, an instantaneous change in the electron density, while an increasing window size flattens out the discontinuity. We now have three clear parameters for controlling the sharpness of the solar eclipse totality spot that are used in this work: 1) the  $h'$  inside the totality spot, 2) the  $\beta$  inside the totality spot, and 3) the smoothing window on the waveguide parameters.

#### 4.1 Estimating the Totality Spot Parameters and Settling Time

The eclipse totality spot will be modified with combinations of  $h'$  from 77 km to 92 km and  $\beta$  from  $0.5 \text{ km}^{-1}$  to  $0.9 \text{ km}^{-1}$ . The third lever, the transition width of the totality spot, is modified by applying a moving average filter, of some window size, on the  $h'$  and  $\beta$  arrays. As previously stated, the daytime D-region electron density is assumed to be homogeneous and constant with a  $h' = 71 \text{ km}$  and  $\beta = 0.43 \text{ km}^{-1}$ .

The left panel of Figure 3 summarizes the FDTD modeling results. The x-axis is the  $h'$  value and the y-axis is the  $\beta$  value. The color represents the  $\Delta H_\phi$  at the receiver location, which is calculated as the absolute value of the difference between the a “typical daytime” D-region electron density and the respective eclipse totality spot run in units of dB-pT, or decibels of picoTesla. Note that  $H_\phi$  corresponds to the major axis length from the observations. The optimal solution is found by finding the configuration of the parameters that produces a back scattered  $\Delta H_\phi$  of about 0.5 dB-pT. As previously stated, the 0.5 dB-pT enhancement is used as the back scattering from the solar eclipse totality spot because it allows for the use of a two-dimensional FDTD model. The optimal configuration of the three-parameters is found to be  $h' = 80 \pm 3 \text{ km}$ ,  $\beta = 0.9 \pm 0.1 \text{ km}^{-1}$ . The error bars for  $h'$  and  $\beta$  are the parameter step sizes used. As the smoothing window is increased, the modeled amount of back scatter quickly decreases and thus these windows are not shown here.

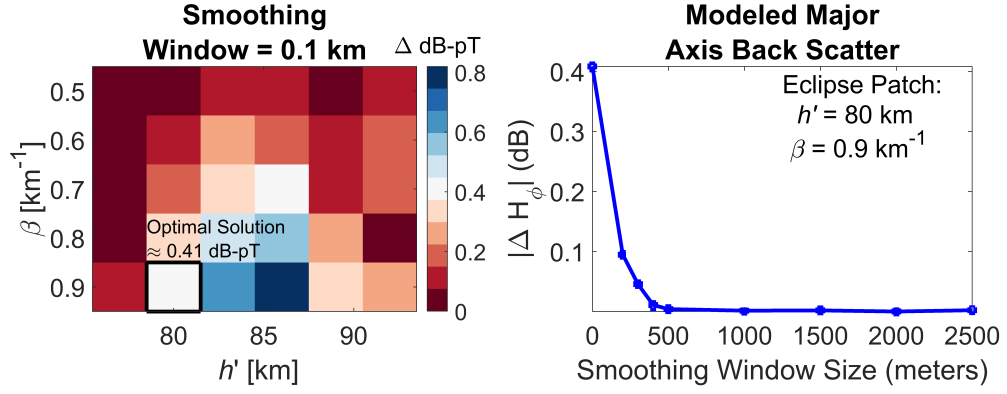


**Figure 3.** Left Panel: Summary of the results of varying the solar eclipse totality spot using  $h'$ ,  $\beta$ , and no smoothing. The color is the absolute value of the difference between a baseline case, i.e. typical daytime propagation, and the back scattered major axis length at the receiver location,  $\Delta H_\phi$ . Right Panel: Absolute value of the back scattered major axis length,  $|\Delta H_\phi|$ , (blue line) as a function of the smoothing window size using an eclipse patch with parameters the  $h' = 80$  km and  $\beta = 0.9$   $\text{km}^{-1}$ .

When the D-region is temporarily perturbed, the steady-state electron density, collision frequency, and other parameters and processes are disrupted for some period of time, e.g. Rodger, Clilverd, and Dowden (2002). The time it takes for the D-region to return to “normal” or recover from the perturbation is called the *settling time*. Specifically, the settling time described in this section refers to the minimum time that the D-region must change to allow for back scattering to occur. During the 21-August-2017 solar eclipse, the totality spot traversing the CONUS created a “known” perturbation, a very rare occasion in geophysics, which is useful for estimating the settling time. To calculate the settling time,  $T_{\text{settling}}$ , the two unknowns that must be determined are: 1) the velocity of the totality,  $V_{\text{totality}}$ , and 2) the width of the transition region of the totality,  $W_{\text{totality}}$ .

Coster et al. (2017) studied the impact of the 21-August-2017 eclipse on the total electron content (TEC) of the ionosphere and found that the “depletion” in the TEC caused by the eclipse moved at approximately the same speed as the totality. The first unknown, the velocity of the totality, is thus simply the velocity of the totality shadow moving along the ground. Thus, the totality spot velocity is assumed to be  $V_{\text{totality}} \approx 0.65 \frac{\text{km}}{\text{s}}$ .

The second unknown is the width of the transition region of the totality spot. The right panel of Figure 3 shows the absolute value of the back scattered major axis length,  $|\Delta H_\phi|$ , as a function of the smoothing window size using an eclipse patch with the parameters  $h' = 80$  km and  $\beta = 0.9$  km<sup>-1</sup>. At a smoothing window size of about 500 meters, the back scattered amplitude approaches zero. The width of this curve is the width of the transition region of the totality spot, thus  $W_{totality} = 500$  km.

The two variables,  $V_{totality}$  and  $W_{totality}$ , are now combined and the settling time is calculated as in Equation 2. Thus, during the 21-August-2017 solar eclipse, the totality spot moving had a settling time of atleast 0.77 s.

$$T_{settling} = \frac{W_{totality}}{V_{totality}} = \frac{0.5 \text{ km}}{0.65 \frac{\text{km}}{\text{s}}} = 0.77 \text{ s} \quad (2)$$

## 4.2 Edge Effect on Back Scattering

Using the optimal parameters for the totality spot, the contribution of each “edge” of the spot to the total back scattered wave can be investigated. In the work above, a smoothing window was applied to the entire eclipse patch. Now, the smoothing window is only applied to half of the spot. This is meant to simulate the totality patch as it moves over the CONUS – the “soft” edge corresponds to the day-to-shadow side of the spot, i.e. the “front” of it, while the “sharp” edge corresponds to the shadow-to-day side of the spot, i.e. the “back” of it. The main assumption here is that the ionization caused by the Sun more of an instantaneous process, while a shadow slows the ionization, but isn’t instantaneous. Figure 4 shows the four possible configurations. The “near edge” indicates the edge of the totality spot closest to the transmitter/receiver, while the “far edge” is the edge away from them. The sloped edge corresponds to a “soft” edge, while the instantaneous edge corresponds to a sharp edge. The four cases are: 1) two sharp edges, 2) a sharp edge on the far edge and soft edge on the near edge, 3) a soft edge on the far edge and a sharp edge on the near edge, and 4) two soft edges.

The modeled back scatter amplitude at the receiver is shown in the top right of each panel. The greatest amount of back scatter is modeled when using two sharp edges for the totality spot followed by using a soft near edge and sharp far edge. Negligible back scatter is detected in the two other cases. The case with the second most back scatter detected, the soft near edge and sharp far edge, is more similar to the totality spot mov-

ing northwest-to-southeast across the CONUS. Since the totality spot is moving diagonally relatively to the predominantly north-south transmitter-to-receiver propagation path, the near edge of the spot would be a day-to-night transition, a soft edge, while the far edge would be a night-to-day transition, a sharp edge. Thus, assuming that the top right panel of Figure 4 is the real case, then the settling time calculated in Equation 2 applies to the far edge of the totality spot.

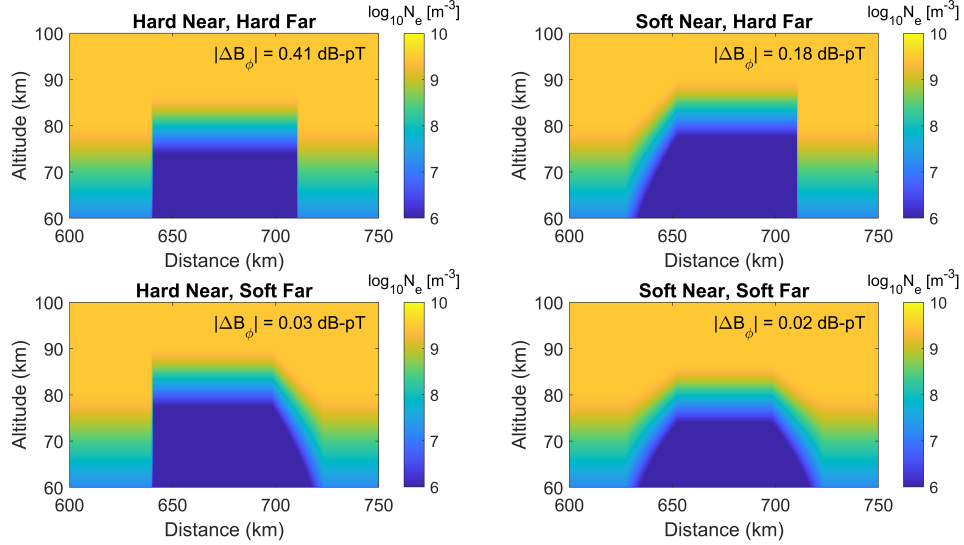


**Figure 4.** Summary from investigating the effect of each edge of the totality spot on the received back scatter using varying smoothing window sizes. The eclipse totality spot parameters used were  $h' = 80 \text{ km}$  and  $\beta = 0.9 \text{ km}^{-1}$  and each edge was as either "hard" or "soft". The color represents the electron density.

The discrepancy in detected back scatter between the two strongest cases, top two panels of Figure 4, can be explained by the error introduced by using a two-dimensional model to explain a three-dimensional phenomenon and by using a stationary model to explain a non-stationary process. The latter is especially meaningful, since, from examining the overall trend of each interference pattern, varying one edge from sharp to soft changes the angle of the back scatter. In the case of a soft near edge and sharp far edge, back scatter of about 0.41 dB-pT can be detected closer towards the transmitter. Thus, in a three-dimensional simulation space, as this totality spot moves to the southeast stronger

back scatter would be detected by the receiver, such as in the case of the two sharp edges and as detected from observations.

## 5 Conclusion

In this paper we present observations of forward and, for the first time, back scattering from the totality spot of the 21-August-2017 “Great American” solar eclipse. An FDTD model is used to estimate the waveguide parameters of the totality spot and the width of the spot transition region required to generate the detected levels of back scatter. The totality spot was found to have an  $h' = 80 \pm 3$  km and a  $\beta = 0.9 \pm 0.1$  km<sup>-1</sup>, with a transition region width of about 500 meters. This corresponds to a settling time of  $T_{\text{settling}} = 0.77$  s, which describes a lower bound on the rate of change of the processes occurring in the D-region required to facilitate back scattering from the totality spot. Finally, the effect of varying the sharpness of the near and far edges of the totality spot is investigated. Although the case with two sharp boundaries generates the most back scatter, the case with a soft near edge and sharp far edge generates an appreciable amount of back scatter and closely emulates the real propagation scenario.

## References

- Belrose, J., Hatton, W., McKerrow, C., & Thain, R. (1959, may). The Engineering of Communication Systems for Low Radio Frequencies. *Proceedings of the IRE*, 47(5), 661–680. Retrieved from <http://ieeexplore.ieee.org/document/4065729/> doi: 10.1109/JRPROC.1959.287236
- Belrose, J., & Thomas, L. (1968, jan). Ionization changes in the middle latitude D-region associated with geomagnetic storms. *Journal of Atmospheric and Terrestrial Physics*, 30(7), 1397–1413. Retrieved from <https://www.sciencedirect.com/science/article/pii/S0021916968912609> doi: 10.1016/S0021-9169(68)91260-9
- Bickel, J. E. (1957, sep). A method for obtaining LF oblique-incidence reflection coefficients and its application to 135.6-kc/s data in the Alaskan area. *Journal of Geophysical Research*, 62(3), 373–381. Retrieved from <http://doi.wiley.com/10.1029/JZ062i003p00373> doi: 10.1029/JZ062i003p00373
- Clarke, C. (1962). Atmospheric radio-noise studies based on amplitude-probability measurements at Slough, England, during the International Geophysi-

- cal Year. *Proceedings of the IEE Part B: Electronic and Communication*  
*Engineering*, 109(47), 393. Retrieved from [http://digital-library](http://digital-library.theiet.org/content/journals/10.1049/pi-b-2.1962.0224)  
[.theiet.org/content/journals/10.1049/pi-b-2.1962.0224](http://digital-library.theiet.org/content/journals/10.1049/pi-b-2.1962.0224) doi:  
10.1049/pi-b-2.1962.0224
- Clilverd, M. A., Rodger, C. J., Thomson, N. R., Lichtenberger, J., Steinbach,  
P., Cannon, P., & Angling, M. J. (2001, jul). Total solar eclipse effects  
on VLF signals: Observations and modeling. *Radio Science*, 36(4), 773–  
788. Retrieved from <http://doi.wiley.com/10.1029/2000RS002395> doi:  
10.1029/2000RS002395
- Cohen, M. B., Gross, N. C., Higginson-Rollins, M. A., Marshall, R. A., Gólkowski,  
M., Liles, W., ... Rockway, J. (2018, apr). The Lower Ionospheric  
VLF/LF Response to the 2017 Great American Solar Eclipse Observed  
Across the Continent. *Geophysical Research Letters*, 45(8), 3348–3355.  
Retrieved from <http://doi.wiley.com/10.1002/2018GL077351> doi:  
10.1002/2018GL077351
- Cohen, M. B., Said, R. K., Paschal, E. W., McCormick, J. C., Gross, N. C., Thomp-  
son, L., ... Chang, J. (2018, sep). Broadband longwave radio remote sens-  
ing instrumentation. *Review of Scientific Instruments*, 89(9), 094501. Re-  
trieved from <http://aip.scitation.org/doi/10.1063/1.5041419> doi:  
10.1063/1.5041419
- Coster, A. J., Goncharenko, L., Zhang, S. R., Erickson, P. J., Rideout, W., & Vier-  
nen, J. (2017, dec). GNSS Observations of Ionospheric Variations During the  
21 August 2017 Solar Eclipse. *Geophysical Research Letters*, 44(24), 12,041–  
12,048. Retrieved from <http://doi.wiley.com/10.1002/2017GL075774> doi:  
10.1002/2017GL075774
- Füllekrug, M., Koh, K., Liu, Z., & Mezentsev, A. (2019, jan). First Map of Co-  
herent Low-Frequency Continuum Radiation in the Sky. *Radio Science*, 54(1),  
44–59. Retrieved from <http://doi.wiley.com/10.1029/2018RS006705> doi:  
10.1029/2018RS006705
- Gross, N. C., Cohen, M. B., Said, R. K., & Gólkowski, M. (2018, jan). Polar-  
ization of Narrowband VLF Transmitter Signals as an Ionospheric Diag-  
nostic. *Journal of Geophysical Research: Space Physics*, 123(1), 901–917.  
Retrieved from <http://doi.wiley.com/10.1002/2017JA024907> doi:

- 10.1002/2017JA024907
- Higginson-Rollins, M. A., & Cohen, M. B. (2017, aug). Exploiting LF/MF signals of opportunity for lower ionospheric remote sensing. *Geophysical Research Letters*, 44(16), 8665–8671. Retrieved from <http://doi.wiley.com/10.1002/2017GL074236> doi: 10.1002/2017GL074236
- Johnson, M. P., Inan, U. S., Lev-Tov, S. J., & Bell, T. F. (1999, aug). Scattering pattern of lightning-induced ionospheric disturbances associated with early/fast VLF events. *Geophysical Research Letters*, 26(15), 2363–2366. Retrieved from <http://doi.wiley.com/10.1029/1999GL900521> doi: 10.1029/1999GL900521
- Kaufmann, P., & Schaal, R. (1968, mar). The effect of a total solar eclipse on long path VLF transmission. *Journal of Atmospheric and Terrestrial Physics*, 30(3), 469–471. Retrieved from <https://www.sciencedirect.com/science/article/pii/0021916968901190> doi: 10.1016/0021-9169(68)90119-0
- Kotovskiy, D. A., & Moore, R. C. (2016, may). Photochemical response of the nighttime mesosphere to electric field heating-Onset of electron density enhancements. *Journal of Geophysical Research: Space Physics*, 121(5), 4782–4799. Retrieved from <http://doi.wiley.com/10.1002/2015JA022054> doi: 10.1002/2015JA022054
- Last, D., & Poppe, D. (1996, dec). A Coverage Prediction Model for Radio Beacon Differential Satellite Navigation Systems. *Navigation*, 43(4), 451–469. Retrieved from <http://doi.wiley.com/10.1002/j.2161-4296.1996.tb01932.x> doi: 10.1002/j.2161-4296.1996.tb01932.x
- Last, J., & Poppe, D. (1997). Effect of skywave interference on coverage of radiobeacon DGPS stations. *IEEE Proceedings - Radar, Sonar and Navigation*, 144(3), 163. Retrieved from [http://digital-library.theiet.org/content/journals/10.1049/ip-rsn{\\\_}19971177](http://digital-library.theiet.org/content/journals/10.1049/ip-rsn{\_}19971177) doi: 10.1049/ip-rsn:19971177
- Marshall, R. A. (2012, mar). An improved model of the lightning electromagnetic field interaction with the D-region ionosphere. *Journal of Geophysical Research: Space Physics*, 117(A3), n/a–n/a. Retrieved from <http://doi.wiley.com/10.1029/2011JA017408> doi: 10.1029/2011JA017408
- Marshall, R. A., & Close, S. (2015, jul). An FDTD model of scattering from meteor head plasma. *Journal of Geophysical Research A: Space Physics*, 120(7), 5931–



5942. doi: 10.1002/2015JA021238
- McCormick, J. C., Cohen, M. B., Gross, N. C., & Said, R. K. (2018, apr). Spatial and Temporal Ionospheric Monitoring Using Broadband Sferic Measurements. *Journal of Geophysical Research: Space Physics*, 123(4), 3111–3130. Retrieved from <http://doi.wiley.com/10.1002/2017JA024291> doi: 10.1002/2017JA024291
- McKerrow, C. (1957). Some Recent Measurements of Atmospheric Noise in Canada. *Proceedings of the IRE*, 45(6), 782–786. Retrieved from <http://ieeexplore.ieee.org/document/4056602/> doi: 10.1109/JRPROC.1957.278475
- McKerrow, C. A. (1960, jul). Some measurements of atmospheric noise levels at low and very low frequencies in Canada. *Journal of Geophysical Research*, 65(7), 1911–1926. Retrieved from <http://doi.wiley.com/10.1029/JZ065i007p01911> doi: 10.1029/JZ065i007p01911
- Nicolet, M., & Aikin, A. C. (1960, may). The formation of the D region of the ionosphere. *Journal of Geophysical Research*, 65(5), 1469–1483. Retrieved from <http://doi.wiley.com/10.1029/JZ065i005p01469> doi: 10.1029/JZ065i005p01469
- Rodger, C. J., Clilverd, M. A., & Dowden, R. L. (2002, jul). D region reflection height modification by whistler-induced electron precipitation. *Journal of Geophysical Research: Space Physics*, 107(A7), 1145. Retrieved from <http://doi.wiley.com/10.1029/2001JA000311> doi: 10.1029/2001JA000311
- Schaal, R. E., Mendes, A. M., Ananthakrishnan, S., & Kaufmann, P. (1970, jun). VLF propagation effects produced by the eclipse. *Nature*, 226(5251), 1127–1129. Retrieved from <http://www.nature.com/articles/2261127a0> doi: 10.1038/2261127a0
- Sprenger, K., Lauter, E., & Schmelovsky, K. (1962, dec). Solar eclipse effects in low and medium frequency propagation. *Journal of Atmospheric and Terrestrial Physics*, 24(12), 1041–1057. Retrieved from <http://linkinghub.elsevier.com/retrieve/pii/0021916962901599> doi: 10.1016/0021-9169(62)90159-9
- Wait, J., & Spies, K. (1964). Characteristics of the Earth-ionosphere waveguide for VLF radio waves.
- Wolfe, D. B., Judy, C. L., Haukkala, E. J., & Godfrey, D. J. (2000). Engineering The World’s Largest DGPS Network. *Control Engineering*, 1 (June), 26–28.

405 Retrieved from <http://ieeexplore.ieee.org/document/881237/> doi:  
406 10.1109/OCEANS.2000.881237

#### 407 **Acknowledgments**

408 This work was supported by the National Science Foundation under grant AGS 1451142  
409 and AGS 1653114 (CAREER) to the Georgia Institute of Technology. The first author's  
410 work was also supported by the NSF Graduate Research Fellowship, DGE-1650044. We  
411 thank Dr. Robert Marshall from the University of Colorado at Boulder for the use of  
412 his FDTD model. Data will be made available through the WALDO repository (<http://waldo.world/>).